Lock-in Pixel Based Time-of-Flight Range Imagers: An Overview

Keita YASUTOMI[†,††a)] *and* **Shoji KAWAHITO**[†,††], *Members*

SUMMARY   Time-of-flight (TOF) range imaging is a promising technology for various applications such as touchless control, augmented reality interface, and automotive. The TOF range imagers are classified into two methods: direct TOF with single photo avalanche diodes and indirect TOF with lock-in pixels. The indirect TOF range imagers have advantages in terms of a high spatial resolution and high depth precision because their pixels are simple and can handle many photons at one time. This paper reviews and discusses principal lock-in pixels reported both in the past and present, including circuit-based and charge-modulator-based lock-in pixels. In addition, key technologies that include enhancing sensitivity and background suppression techniques are also discussed.
key words: time-of-flight, CMOS image sensors, lock-in pixel, 3-D imaging, charge modulator

Fig. 1   Principle of TOF distance measurment.

1.   Introduction

Over the last two decades, numerous innovations in solid-state imaging devices have changed our lifestyle by making digital cameras more available. This growth has also driven the development of 3D imaging, and many depth cameras are becoming more accessible and pervasive in our lives. Among many 3D imaging technologies, time-of-flight (TOF) range imaging has attracted much attention because of the capability of its small form factor, low cost, and real-time acquisition for various applications such as touchless control, augmented reality interface, and automotive.

TOF range cameras [1] obtain a depth image as well as an intensity image by sensing a round-trip time from a light source to an object, as shown in Fig. 1. The distance, D, is calculated by the time of flight, t_{TOF}, and the known light of speed, c, as the following equation.

$$D = \frac{c}{2} t_{TOF}. \tag{1}$$

The TOF ranging system with a scanning mechanism is also called light detection and ranging (LIDAR).

The TOF measurement is divided into two methods: direct TOF (dTOF) and indirect TOF (iTOF) shown in Figs. 2 (a) and 2 (b), respectively. The dTOF uses a short pulse laser and directly measures the TOF using
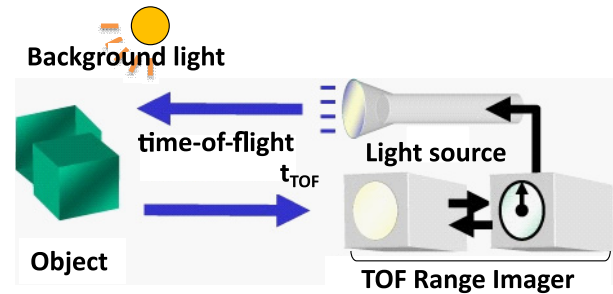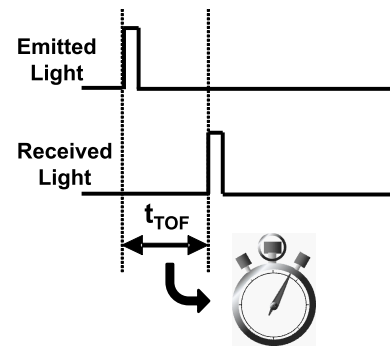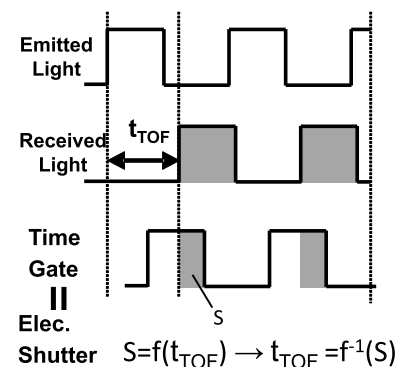

(a) direct TOF (dTOF)

$S = f(t_{TOF}) \rightarrow t_{TOF} = f^{-1}(S)$

(b) indirect TOF (iTOF)

Fig. 2   TOF measurement method

time-measurement circuits such as time-digital converters (TDCs). In order to generate the STOP signal of the time-measurement circuits, single-photon avalanche diodes (SPADs) [2]–[5] are widely used as the detectors of CMOS dTOF imagers. The SPAD is an avalanche photodiode operated in a Geiger mode having an infinity avalanche gain, and generates a pulse associated with an incident photon.

The dTOF imagers exhibit an excellent performance at long distance measurement owing to their high-sensitivity nature [3], [4], [6]. On the other hand, the dTOF imagers require a TDC implementation basically on a unit pixel. The shared TDC architecture [4], [6] relaxes the requirement at the cost of non-simultaneous acquisition for all pixels, and the stacked technology [4], [6] prevents the deterioration of the fill factor of SPADs. However, the spatial resolution is still limited to 65k pixels [4] and 0.1M pixels [6] as dTOF imagers. The recent progress in-depth for SPADs and dTOF imagers is summarized in [7].

Another approach is iTOF measurement that uses a time gating corresponding to a fast electronic shutter, as shown in Fig. 2 (b). The iTOF pixels accumulate photo-generated charges within the time gate into in-pixel storage. Such the pixel used in iTOF imaging is called lock-in pixel [8]. The time gate in the lock-in pixels is synchronized with the light, enabling the acquisition of a time-dependent signal (denoted as S in Fig. 2 (b)). The change of TOF, t_{TOF}, in time domain is converted to changes in amplitude of the accumulated signal as a function f: $S = f(t_{TOF})$, and the TOF is deduced by the inverse function: $t_{TOF} = f^{-1}(S)$. The readout scheme of the lock-in pixel based on charge modulators, described in Sect. 3, is similar to that of CMOS image sensors. Since the required in-pixel transistors of lock-in pixels are less than that of dTOF imager, iTOF imagers is suitable for higher spatial resolution. Solid-state TOF range cameras with lock-in pixels were launched commercially in the early to mid-2000s by PMD Technology, MESA Imaging, and Canesta. In 2014, Microsoft released Kinect V2 [9] having 0.2M pixels in several hundred dollers for gaming applications. This led to the production of QVGA- and VGA-sized depth cameras by many manufacturers. Recently, Microsoft has released the 1M pixels iTOF camera, Azure Kinect [10]. The launch has been followed by the publication of high-resolution iTOF imagers [11], [12].

The other advantage of iTOF imagers with lock-in pixels is the capability of handling many photons at one time. In outdoor conditions, high background light (BGL) due to the sunlight causes issues of saturation and deterioration of depth precision. The charge-modulator-based lock-in pixel with BGL suppression circuits has the potential to be more resistant to BGL. Furthermore, the feature of handling multiple photon capability also exhibits high depth precision up to 67 μm [13] that is expected to be applicable to 3D scanning systems for component inspection and reverse modeling.

The aim of this paper is to provide an overview of the recent iTOF range imager design. This paper reviews and discusses principal lock-in pixels reported both in the past and present, including circuit-based and charge-modulator-based lock-in pixels. Section 2 describes the basic principle of iTOF range imaging, and the essential element, lock-in pixels, are discussed in Sect. 3. In Sect. 4 describes key technologies for present and next-generation iTOF imagers that enables outdoor use. Finally, the conclusion is presented in Sect. 5.

2. Indirect TOF Imaging

2.1 Modulation Methods in Indirect TOF

The iTOF methods are classified according to the driving method of light source: continuous wave (CW) or short-pulsed (SP) illumination, as shown in Fig. 3. In the CW-iTOF method, a sinusoidal or pulsed illumination with 50% duty is demodulated by time gates with different phases. The phase shift, ϕ_{TOF}, is calculated by those accumulated signals. When the light pulse is the sinusoidal with a modulation frequency, f_m, and it is demodulated by four-tap time gates (G1-G4), the phase shift and the TOF are calculated by

$$\phi_{TOF} = \arctan\left(\frac{N_2 - N_4}{N_1 - N_3}\right) \qquad (2)$$

$$t_{TOF} = \frac{1}{f_m}\left(\frac{\phi_{TOF}}{2\pi} + k\right) \qquad (3)$$

where N_1-N_4 are the signal electrons acquired by G1-G4, and k is an integer. Although the acquired signals contains unwanted signals due to a BGL and unmodulated photogenerated signal, taking difference between two phase signals, i.e. $N_1 - N_3$ or $N_2 - N_4$, cancels those unwanted component except for their shot noises.

In the actual iTOF imagers using CW-iTOF method, 2-tap pixels [9], [14]–[16] are frequently used instead of 4-tap ones [8], [11], [17]. The 2-tap pixel obtains the four different phase signals using two consecutive frames in which the phase of the light source is changed. The choice of 2-tap lock-in pixels simplifies the pixel design at the cost of halve frame rate and less robustness concerning a motion artifact of moving objects. According to [1], (3) is derived from the definition of discrete fourier transform (DFT). In DFT with N sample points, $N/2 - 1$ discrete frequency component is only deduced. In the ideal CW-iTOF, a single frequency is used. This means that $N = 4$, i.e., $N/2 - 1 = 1$, is sufficient to deduce the phase delay. Therefore, a multi-tap lock-in pixel of more than 4 taps is unnecessary in CW-iTOF.

Since CW-iTOF measures the phase shift, which has a duplicate value in every 2π cycle, causing phase wrapping that is represented as k in (3). The phase wrapping causes an ambiguity of depth calculation. This issue comes up to the surface as the modulation frequency increases for higher depth precision. For example, 100-MHz modulation frequency yields an unambiguity range only up to 1.5 m. Thus, an object placed at 2.0 m is misled to 0.5 m. Since Kinect V2 [9] uses a 130-MHz modulation frequency at maximum, solving the issue is essential. A phase unwrapping or ambiguity-resolved technique using multiple frequencies is proposed in [18], [19]. In Kinect V2 [9], three modulation frequencies are used for solving ambiguity. An in-depth description including other phase-unwrapping techniques is summarized in [20].

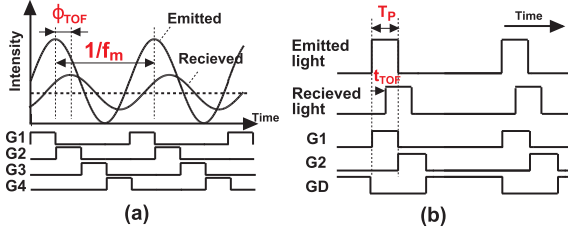In SP-iTOF method, the short pulse with a small duty

Fig. 3 iTOF principle. (a) Continuous wave illumination, CW-iTOF, (b) Pulsed illumination, SP-iTOF.

cycle is used unlike the CW-iTOF. Figure 3 shows an timing example using a 3-tap lock-in pixel (G1-G3) with draining function (GD). The pulse duration of light and time gate are set to be the same (T_P). The photogenerated charges within GD set to high are discarded. In the condition of $0 < t_{TOF} < T_P$, the t_{TOF} is calculated by

$$t_{TOF} = T_P \frac{N_2 - N_3}{N_1 + N_2 - 2N_3} \tag{4}$$

Since N_3 corresponds to the unwanted signal due to BGL, the denominator ($N_1 + N_2 - 2N_3$) represents the signal associated with all of the received light except the BGL. Hence, the signal charge ratio, $\frac{N_2 - N_3}{N_1 + N_2 - 2N_3}$, takes a value from 0 to 1, corresponding to the normalized delay with respect to the pulse width. As decrease the duty ratio while keeping average light power, i.e., increasing the peak power, the robustness to the ambient light increases because the acquisition of the BGL component becomes small in the SP-iTOF. Similar to the CW-iTOF method, 2-tap lock-in pixels using two consecutive frames perform the TOF calculation while removing the BGL component. 3-tap lock-in pixels enable the TOF calculation, excluding the BGL component in a single frame.

Unlike in the CW-iTOF, the unambiguity issue is avoidable to set the duty cycle to be small. For example, a condition of 10-ns pulse with 5% duty results in 200-ns cycle time, corresponding that ambiguity occurs every 30 m that does not matter in reality. The short-pulse width leads to better depth precision but decreases the measurable range. To extend the measurable range, a range-shift technique using multiple frames is presented [21]. In the technique, the trigger delay of the light source is varied in several frames, which is equivalent to shifting of the measurable range. The technique allows the expansion of measurable range while keeping depth precision at the cost of a reduced frame rate. SP-iTOF with multi-tap lock-in pixels [22]–[24] obtains a similar benefit without reducing frame rate, described later.

2.2 Depth Precision

Depth results calculated from iTOF sensor outputs fluctuates due to various noises, and the standard deviation (1σ) is called as depth precision, uncertainty, or range resolution.

The theoretical depth precision can be derived using the error propagation equation to (3),(4). Many works of literature describe theoretical precisions under their condition,

e.g., [1], [25]. Here, we would like to give a basic understanding of the dependency of sensor/system parameters on depth precision.

The depth precision, σ_D, both for CW- and SP-iTOF are given by

$$\sigma_D \propto \frac{D_{MAX}}{C_D} \frac{1}{SNR}$$
$$\propto \frac{D_{MAX}}{C_D} \cdot \frac{\sqrt{\overline{N_S} + \overline{N_{BG}} + \alpha N_R^2}}{\overline{N_S}} \tag{5}$$

where $\overline{N_S}$, $\overline{N_{BG}}$ and $\overline{N_R}$ are a sum of effective signal charges, BGL signal charges, and a dark noise in electrons, respectively. α is a prefactor of dark noise that is determined by readout architecture. The C_D is a demodulation contrast or modulation contrast that is the ratio of modulated signal and offset. The last part in (5) corresponds to SNR^{-1}. In its numerator, the first and second terms in square root represent the shot noises due to signal light and BGL, respectively. The measurable range, D_{MAX}, is determined by

$$D_{MAX} = \begin{cases} \frac{c}{2f_m} & \text{if. CW} - \text{iTOF} \\ \frac{cT_P}{2} & \text{if. SP} - \text{iTOF} \end{cases} \tag{6}$$

The dominant factor in precision is different for applications. Here, we consider the following three cases:

- Case 1: high light condition with less BGL: non-mobile, indoor use, and short-range application.
  This case gives an asssumption: $\overline{N_S} \gg \overline{N_BG}, N_R^2$, resulting in $SNR = 1/\sqrt{N_S}$. The depth precision at this condition is intrinsic limit of TOF range measurement. For better precision, reducing D_{MAX} or increasing N_S is required. Since the improvement of precision by increasing N_S is proportional to the square root of N_S, reducing D_{MAX} is efficient. Reducing D_{MAX} corresponds to high modulation frequency in CW-iTOF or short pulse width in SP-iTOF. While the D_{MAX} can be extended; the phase wrapping issue due to high modulation frequency is solved using the multiple frequency techniques, and the limited D_{MAX} is extended by range shift technique using multiple frames or multi-tap lock-in pixels in the SP-iTOF.

- Case 2: limited light power condition with less BGL such as mobile applications at indoor use.
  This case suppose that $\overline{N_{BG}} \simeq 0$ and N_R^2 comparable to $\overline{N_S}$. Thus, the dark noise associated with the readout circuits becomes a dominant factor in the depth precision. Obtaining lower dark noise, kTC noise canceling is effective. For this purpose, the implementation of in-pixel intermediate storages is adapted in [10], [17], [26]. Since the choice often reduces the full well capacity, a higher modulation frequency is essential to reduce D_{MAX}. Also, [9], [12] implements a binning function to obtain better precision at the cost of reducing spatial resolution.

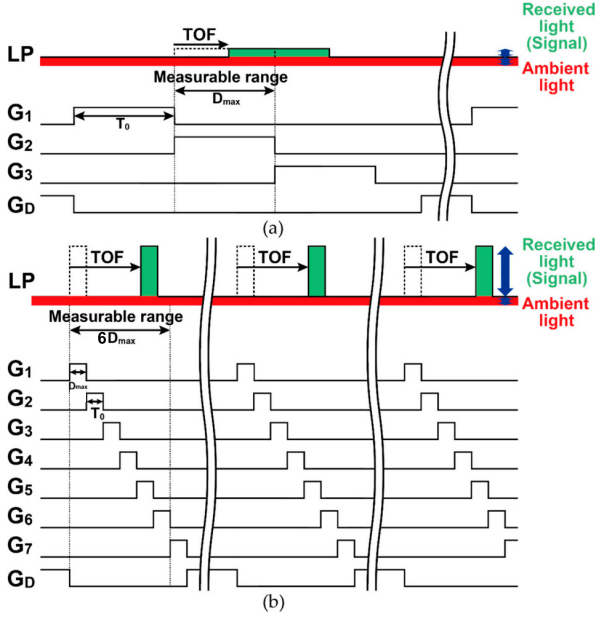- Case 3: high BGL condition such as outdoor use.

Fig. 4 SP-iTOF measurement with a multi-tap lock-in pixel. (a) 3-tap for one time-zone, (b) 7-tap for six time zone.

In this case that supposed to $\overline{N_{BG}} >> \overline{N_S}, \overline{N_R^2}$, the depth precision is given by

$$\sigma_D \propto \frac{D_{MAX}}{C_D} \cdot \frac{\sqrt{\overline{N_{BG}}}}{\overline{N_S}}. \tag{7}$$

In this case, the reduction of BGL is necessary for better depth precision. In this condition, SP-iTOF method obtain better performance using a smaller duty cycle. Another key point is the choise of light wavelength. The spectral irradiance of sunlight becomes lower at longer wavelength due to an absorption of air. For example, the power density at 940-nm is lower than that at 860-nm by a factor of 2.3.

2.3 SP-iTOF with Multi-Tap Lock-in Pixels

Multi-tap lock-in pixels that allow multiple time gates in single capture offer a wide measurable range without any negative effects on depth precision and robustness to motion artifact. Figure 4 shows the SP-iTOF methods using 3-tap and 7-tap lock-in pixels [23]. Here, the measurement range corresponding to one pulse width (T_P) is called time zone. In Fig. 4 (a), the depth calculation performs using the signal ratio between G2 and G3 only. On the contrary, the depth calculation using 7-tap lock-in pixels enables the depth calculation for six time zones in a single frame, as shown in Fig. 4. The D_{MAX} of 7-tap lock-in pixels is six times smaller than that of 3-tap lock-in pixels. Hence, 7-tap lock-in pixels gives six times better precision compared to 3-tap lock-in pixel, while keeping the measurable range. In addition to this, the BGL signals are also reduced in the method.

An efficient timing operation, which is called a depth-adaptive time-gating-number assignment, was also proposed in [23]. For the wide-range distance measurement, the difference of reflected photons between distances in short and long causes an issue; since the reflected photons of short-range are much larger than that of long-range, saturation is more likely to occur in short distances. In [23], the number of accumulation for each time gate (G1-G7) were adjusted so that the reflected photons (from targets having the same reflectivity) are equal for all measurement range. The effectiveness of those techniques was clearly demonstrated in [23].

3. Lock-in Pixel

3.1 Histrical Overview

So far, numerous lock-in pixels have been presented. The lock-in pixels are classified into two categories: charge-modulator-based and circuit-based lock-in pixels. In the 1990s, charge-modulator-based lock-in pixels that were fabricated by CCD or CCD-CMOS technology were presented [8], [14], [27], [28]. In the early 1990s, CCDs were predominated as solid-state imaging devices. However, CMOS image sensors had been actively developed at the time because of their attractive feature: high functionality, low power consumption, and cost-effectiveness [29]. For these reasons, charge-modulator-based lock-in pixels in standard CMOS technology were also investigated [30], [31]. Through these developments, solid-state TOF range cameras were commercialized by PMD technologies, MESA imaging, and Canesta in the early and mid-2000s.
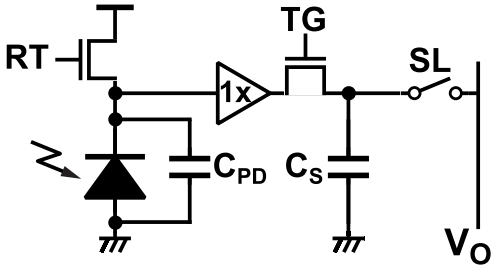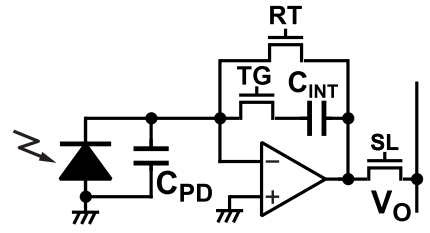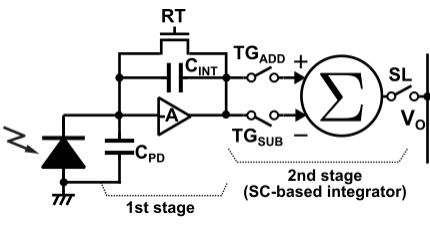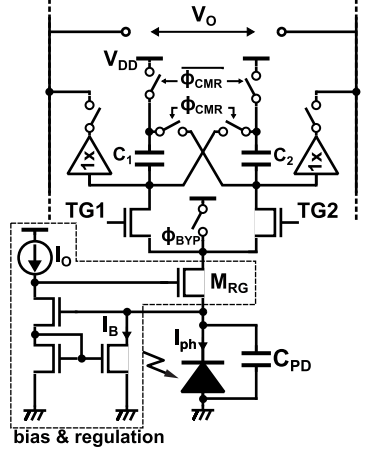
On the other hand, circuit-based lock-in pixels were also investigated in the academic field from the early 2000s [32]. Circuit-based lock-in pixels have several strengths: (1) implementable on a standard CMOS process, (2) easy implementation of BGL suppression, that is because the polarity of charge summation is easily switchable. However, the circuit-based lock-in pixels suffer from noise accumulation during repeated accumulation, while the charge-modulator-based lock-in pixels enable noise-free accumulation. Also, the complicated pixel circuits lead to pixel size limitation or lower spatial resolution. As a result the charge-modulator-based lock-in pixels are more prevalent than the circuit-based ones these days.

In the next subsection, we briefly review the circuit-based lock-in pixels. The further detailed discussion, including case studies, is described in [33].

3.2 Circuit-Based Lock-in Pixel

Circuit-based lock-in pixels are summarized in Table 1. In the early stage, the buffer and sampling type was presented [32]. The concept is very simple; after RT (reset) turns off, the photocurrent due to the incident light integrates on C_{PD}, and the resultant voltage is buffered and sampled

Table 1 Summary of circuit-based lock-in pixels. In the figures, RT and SL stand for reset and select signals, respectively. TG including TG_{ADD}, TG_{SUB}, TG1 and TG2 stands for time gate signal, corresponding to electronic shutter shown in Fig. 3.

Circuit topology	Simplified example	Remarks
Buffer type		• Simple & less circuit component (opamp is not required.) • Low sensitivity (The conversion gain is determined by C_{PD}) • No repeated accumulation at pixel level • No CDS (kT/C noise remains) • Power hungry Presented in [32, 34] where background suppression and repeated accumulation is implemented in column readout circuits.
SC-integration		• Sensitivity improved by charge amplification (The conversion gain is determined by C_{INT}) • Repeated accumulation • Background suppression can be implemented by fully-differential topology with a dummy photodiode. • No CDS (kTC noise remains) Fully-differential pixels using a dummy photodiode are presented in [35, 36].
Two-stage SC-intageration		• Sensitivity improved by charge amplification [38] (The conversion gain is determined by C_{INT}) • Repeated accumulation • Background suppression is implemented by fully-differential approach. • True CDS (kTC noise on C_{PD} is cancelled.) • Large power consumption • Complicated topology Presented in [37, 38]
Photocurrent modulation		• Repeated accumulation is available • Low power consumption • BGL suppression • No CDS and additional noise due to the bias current Presented in [39–41]

into C_S using TG (time gate) clock. The time gating is determined by the falling edges of RT and TG. In the actual implementation [32], [34], the C_S is followed by the second buffer and another sampling capacitor in order to enable sample and hold operation in the pixel. The pixel is simple and less circuit components compared to other circuit-based lock-in pixels. However, the pixel suffers from low sensitivity, kT/C noises induced at each accumulation, and no repeated accumulation in the pixel level.

In SC-integration lock-in pixels, a switched-capacitor

integrator is used for in-pixel repeated accumulation. The time window is determined by TG, while the photo-charges are drained by RT on. The actual implementation uses a fully differential with a dummy photodiode presented in [35], [36]. Using the dummy photodiode, one side of the fully differential terminals integrates the photocurrent only due to BGL; the BGL suppression is also available. Furthermore, owing to the charge amplification, the charge-voltage conversion gain is determined by C_{INT} that is designed to be smaller than C_{PD}, the sensitivity is improved compared to the buffer-type lock-in pixels. However, the repeated accumulation integrates the kTC noise on C_{INT} as well as photo-generated signals.

For lower noise, two-stage SC-integration lock-in pixels are useful [37], [38]. In the pixel, the amplified or buffered signal at the first stage is added with switchable polarity into the second stage using TG_{ADD} and TG_{SUB}. The second stage is composed of the switched capacitor circuits. In [37], a fully differential buffer is used as the first stage in order to switch the polarity of summation at the second stage. The difficulty of the lock-in pixels is the requirement of many transistors to implement the circuits and power consumption to implement the two amplifiers. In particular, the second stage requires offset calibration to avoid unwanted signals during the repeated accumulation. The calibration circuit is also implemented in the pixel, leading to less fill factor or large pixel size.

The other lock-in pixels based on photocurrent modulation were also presented [39]–[41]. TG1 and TG2 pulse switches the flow of photocurrent (I_{ph}), and those currents are integrated on capacitors: C_1 and C_2. The concept was presented in [42], [43] in 1999. However, it is difficult to apply it to TOF range imaging because the photocurrent is too small and the loss of the current integration occurs due to the parasitic capacitance at the photodiode (C_{PD}) during the repeated accumulation. For reducing the loss, the bias and regulation circuits shown in Table 1 were presented [41]. The regulation circuit makes M_{RG} flowing a constant bias current being the same as I_0. Because of the constant bias current, the voltage of the photodiode is regulated to a fixed voltage, the loss due to C_{PD} is reduced. Although the bias current induces a common-mode signal accumulated on C_1 and C_2, the in-pixel common-mode rejection circuit cancels the common-mode signal, including the current due to BGL. Since the bias current is designed to be small (2 μA), the pixel has low power consumption. The pixel, however, suffers from kTC noises and noises due to the constant bias current, which accumulates on the capacitors during the repeated accumulations.

3.3 Charge-Modulator-Based Lock-in Pixel

The charge modulator is the device enabling an electronic shutter in a short time. In other words, photogenerated electrons moving into a specified storage region within a short time window in the order of several ns to several tens of ns. They perform noise-free repeated accumulation, unlike the circuit-based lock-in pixels. The charge modulator is also called a (photonic) demodulator or a photonic mixing device (PMD).

Figure 5 summarizes the device structures and their potential diagram of charge modulators. The quantitative comparison for those device structures are interesting but difficult. One of the performance parameter is modulation contrast or demodulation contrast at the same frequency or pulse width. However, the contrast depends not only on charge modulation speed, but also on the pulse shape and wavelength of light source, the shape of gate driving pulse that strongly depends on pixel counts. Hence, this section gives each features of charge modulators.

Figures 5 (a) and 5 (b) show the charge modulators using photogate [8], [30], [44], [45] and photogate with buried channel [14], [15], [25], [46], respectively. Those structures are basically identical to the surface- and buried-channel CCDs. The channel potential varies due to the applied gate voltage, and different voltages are applied to the gates (G_1 and G_2) to create the lateral electric field from right to left and vice versa. To realize them in CMOS technology, however, applied voltages to the gates should be reduced to around 3 V while over 10 V is used in CCD technology.

In the buried-channel photogate structure, the fringing field at the gate edges is higher than that of the surface-channel because the equivalent oxide thickness becomes thick; thereby, a smooth lateral electric field is easily obtained. Kawahito et al. presented the photogate structure using CMOS technology [25]. The photogate is formed on the field oxide, and an n-type layer is doped under the photogate to built the buried channel. The thick oxide layer and buried channel enhance the lateral electric field, and 15-μm pixel pitch, 336×252-array TOF imager was demonstrated in 2007.

Figure 5 (c) shows another charge modulator using the pinned photodiode with transfer gates [47]–[50]. In the late 1990s and early 2000s, the pinned photodiode [51], [52] that is one of the most important technology in CCD image sensors was also introduced into CMOS image sensors [53]. The pinned photodiode gives attractive features: a low dark current, the capability of complete charge transfer, and a high full well capacity while keeping a wide depleted (sensitive) region. Among them, the complete charge transfer enables noise-free charge modulation. In the structure, the enhancement of lateral electric field for charge modulation is one of important challenges for TOF range image sensors. This is because the lateral electric field is created only by the fringing field due to the MOS transfer gates at the side of the photodiode. The pinned photodiode region has inherently a constant potential when its size is large (>5-10 μm depending on impurity concentration of the epi layer). For example, in [48], 1-tap lock-in pixel with 12×12 μm^2 was presented; however, the modulation frequency used is only 5 MHz. Kim et al. present another example [50] that has a 6 μm pitch modulator with 70% modulation contrast at 10 MHz in 2012.

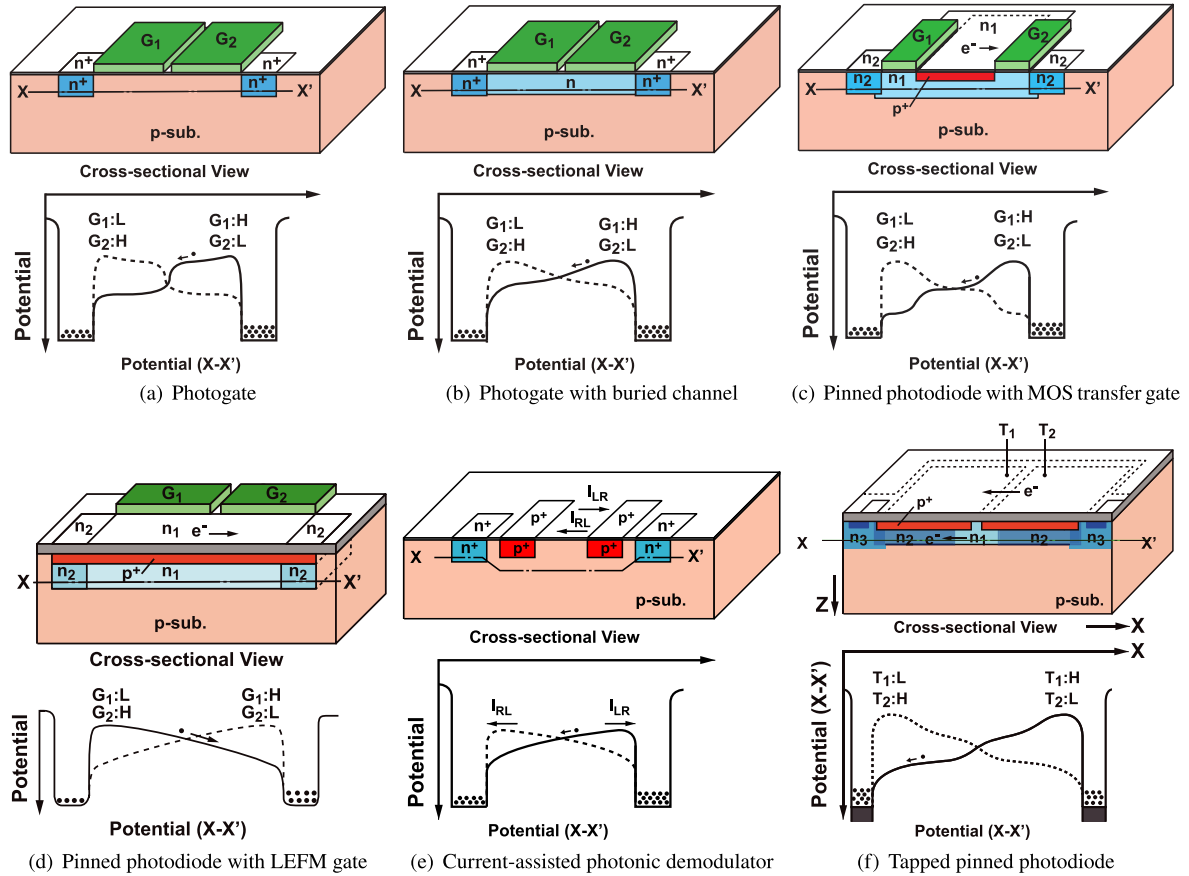Figure 5 (d) shows another pinned photodiode based

Fig. 5 Charge modulators

strcuture for high-speed charge modulation using a lateral electric field modulation (LEFM) gate [13], [22], [54], [55]. In the structure, modulation gates are formed along with the pinned photodiode. The gates varies hole concentration of the surface p-layer of the photodiode, creating a lateral electric field in the channel region. The LEFM structure is conceived from a draining-only modulator (DOM) [56]– [59] that has a modulation gate along with the pinned photo-diode. Since both LEFM and DOM structure has no trans-fer gates on the channel that is the path of signal charges, the smoothly-gradient potential is created, resulting in high-speed charge modulation. There are a wide variety of imple-mentation was presented: a 3-tap with drain [13], [55], 4-tap LEFM with drain [22], 2-tap and 4-tap LEFMs with storage diode [60], [61], and 8-tap (or 7-tap with drain) LEFM [23]. In [22], the 4-tap LEFM with 77% modulation contrast at 20-ns gate pulse is achieved.

Figure 5 (e) shows a current-assisted photonic demodu-lator (CAPD) [62], [63]. In the structure, a current of ma-jority carriers flowing between two p+ region creates the lateral electric field. Unlike other charge modulators, a con-stant current flows during the modulation. However, the cre-ation of a lateral electric field is easy even when the modu-lator size is large. Since the large modulator size increases the resistance between the p+ regions, the constant current is reduced. Thus, the structure is suitable for a relatively

large pixel design. The structure was implemented in stan-dard CMOS technology with front-side illumination [62]. In 2017, Sony and SoftKinetic presented a 320×240-array CAPD TOF sensor with BSI 10-μm pixel pitch [16], [64], demonstrating 80% modulation contrast at the 100-MHz modulation frequency.

Figure 5 (f) shows a tapped photodiode (TPD) modula-tor [65]. Unlike the standard pinned photodiode, surface p+ layers are isolated from the substrate by n-layers such as n_1 and n_2. Each of these p+ layers has its own electrode, and by applying high and low voltage, a lateral electric field is created. Unlike the modulators with the transfer and LEFM gates, the structure directly modulates the channel potential at the central region of the photodiode, and high-speed car-rier transfer is obtained. In [66], a 4-tap TPD modulator has demonstrated a high modulation contrast over 90% with an 8-ns light pulse (850-nm wavelength).

Static-field photodiode structure [67] is preferred to a large pixel design. One of the example is shown in Fig. 6 [68]. At a photogenerated charge at the photodiode is quickly transferred to the modulation diode (MD) and then is transferred to FDs by the transfer gates (G1-G4). In [68], 4-tap pixel having 11.2 μm modulator pitch demonstrated a 4-ns pulse modulation. The concept was first introduced in [67] that uses multiple photogates in 2006. The photo-gates is biased by multiple voltages generated by a resistor
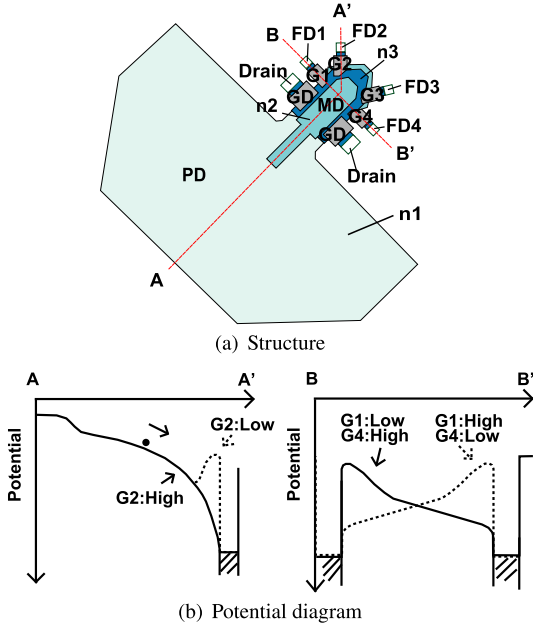
(a) Structure

(b) Potential diagram

Fig. 6   Pinned-photodiode-based Static-Drift-field Modulator

Fig. 7   Calculation results of modulation characteristics when T_P and σ_{cm} are set to be 5 ns and 1 ns. The outputs, N1-N4, and their summation (N_{sum}) are calculated from the convolution of I_{ph} and gate pulses having a perfect square wave. The SP-iTOF with the 4-tap lock-in pixel is emulated for the timing.

ladder. Using a pinned photodiode with various engineered widths, high-speed carrier transfer structures [47], [69] were presented in 2009 and 2010. Recently, Lee et.al. presented trident-shaped pinned photodide [70], which demonstrated a modulation contrast of 61.2% at 100-MHz modulation frequency [70], [71] using BSI technology.

Charge modulators using a vertical overflow drain shutter were presented [72], [73]. The VOD shutter was commonly used in interline-transfer CCD image sensors. The VOD shutter act as drain (inverse of time gate) and transfer gates are used to acquire signal charges. Although 4-tap readout is implemented [73], one-tap signal is only obtained in single exposure. However, high-speed shutter operation up to 5 ns is achieved with high modulation contrast. The structure is also effective to reduce gating clock skew because of its relatively small load capacitance [52].

Recently, lock-in pixels having a small size of 2-3 μm pitch [10]–[12], [26] were presented for a high spatial resolution iTOF sensor having 1-1.2M pixels. Those designs aim to cover a wide field of view and target a distance up to 5 m, mainly for indoor applications. Those designs have binning function such as 2×2 in [10], 4×4 in [12]. Such sensors with small pixel size require advanced fine-pitch technology such as 65nm BSI [10], 65nm/45nm BSI stacked CMOS [12], 65nm BSI stacked technology [11].

3.4   Requirement of Impulse Response for Charge Modulators

When the impulse response of charge modulators is modeled as Gaussian function, the modulator response, $h(t)$, is expressed by

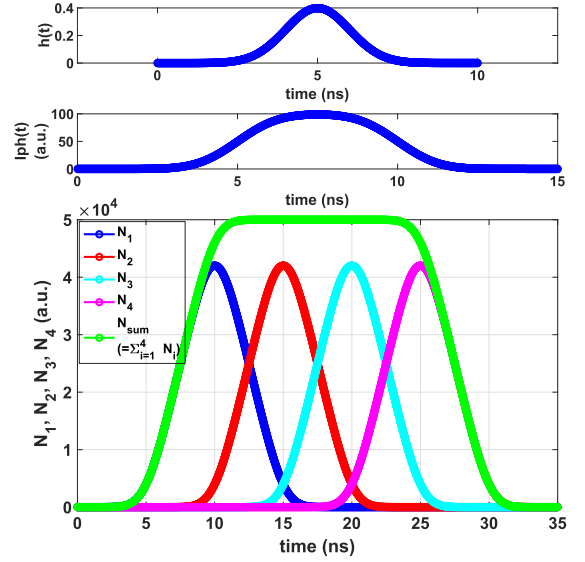$$h(t) = \frac{1}{\sqrt{2\pi}\sigma_{cm}} \exp\left\{-\frac{t^2}{2\sigma_{cm}^2}\right\} \qquad (8)$$

where σ_{cm} is an intrinsic response time of modulators. Although this assumption is not always valid, a similar response has been observed with the pixels that are dedicated to high-speed modulation [13]. A similar assumption is also discussed in the ultra-high-speed imagers [74]. Figure 7 shows calculation results of modulation characteristics when T_P and σ_{cm} are set to be 5 ns and 1 ns. The light and gate pulses are assumed to be a perfect square wave in the calculation, and those widths are the same. The photocurrent, I_{ph} is calculated from the convolution of h(t) and the light pulse. The outputs, N1-N4, and their summation (N_{sum}) are calculated from the convolution of I_{ph} and gate pulses. The SP-iTOF with the 4-tap lock-in pixel is emulated for the timing. The outputs, N1-N4, and their summation (N_{sum}) are calculated from the convolution of I_{ph}. The modulation contrast between the 2 taps ($= \max\left[\frac{|N_2-N_3|}{N_1+N_2+N_3+N_4}\right]$) is 78%. The calculated modulation contrast is equivalent to a 2-tap CW-iTOF one where the modulation frequency is $f_m = 1/(2T_P)$, i.e., 100 MHz for this condition. Figure 8 shows the calculation results as function of T_P/σ_{cm}. To obtain the modulation contrast of >90%, the intrinsic response (σ_{cm}) should be 1/10 than T_P.

The response of the charge modulators is determined mainly by two mechanisms: (1) charge collection from deep substrate and (2) charge modulation due to the lateral electric field. Since the current TOF imagers utilize NIR light such as 940-nm and the size of recent iTOF pixels shrink, the charge collection determined by the vertical electric field is more important. The theoretical limitation of the intrinsic response ($\simeq \sigma_{cm}$) at BSI imagers is discussed in [74]. When the substrate thickness is the same as the absorption length (δ in [74], e.g., 43.5 μm at 940-nm wavelength) and the substrate is biased for the creation of a large and constant ver-

tical field of 2.5×10^4 V/cm at which the carrier velocity is 9.19×10^{-2} μm/ps, the intrinsic response (1σ) is $3.06\delta \simeq 133$ ps at 940-nm wavelength. Although the calculation does not consider a finite modulation time in any lateral directions and the finite response of gate/light pulse, this indicates that charge modulators themself have a potential to achieve 375-MHz modulation frequency, 90% modulation contrast, and internal QE of 63%.

3.5 Storage Design

The iTOF imagers basically require global shutter (GS) operation unlike rolling shutter operation, which is used in typical CMOS imagers. The readouts for charge-modulator-based lock-in pixels are typically the same. The FD is typically used as charge storage. Since this configuration yields uncorrelated double sampling for readout, the kTC noise at FDs remains. In the same manner as two-stage charge-transfer GS pixels [75], [75], [76], implementing in-pixel charge storages allow CDS operation for lower readout noise. Those lock-in pixels were reported in [60], [61], [77] for other lock-in pixel applications such as fluorescence life-time imaging. As described in Sect. 2.2, the influence of readout noise to depth precision depends on operating conditions. For mainly indoor use, recent TOF imagers having small pixel size [10], [17], [26] implement the in-pixel charge storage, achieving a low noise level of around 3.5 e-. However, those pixels have the limited full well capacity of several ten ke- (e.g., 20ke- in [26]).

For outdoor use in which both high and low BGL conditions exist, both low noise and high dynamic range are important. One of the choices to obtain the performance is double-delta correlated multiple sampling (DD-CMS) [78], [79]. Although it requires a 2x readout sequence in a single frame, a relatively low noise level is obtained. In [79], DD-CMS readout allows 5x noise reduction, and the noise level of 15 e- with a conversion gain of 8.3 μV/e is obtained. Another possibility is a readout using switchable

conversion gain such as lateral overflow integration capacitors (LOFICs) [80], [81]. Although the implementation of additional capacitors is required, the stacked CIS technology, especially pixel-parallel connection [12], [76], may resolve the issues.

4. Key Technologies and Discussions

4.1 Enhancing Sensitivity for NIR Region

High sensitivity to NIR light is essential for TOF range imagers because the light source power is limited due to eye safety. Longer wavelength has a smaller absorption coefficient of light; it penetrates deeper Si substrate. When the light is absorbed outside of the depletion region, the photo-generated electrons move around by diffusion mechanism. Although some of them come to the photodiode region, the collection speed is not acceptable in TOF range imagers. Therefore, the TOF sensors should have a thick substrate with wide depleted region both for increased NIR sensitivity and high-speed charge collection.

Figure 9 shows the calculation results of internal QE for three NIR wavelengths: 860, 900, and 940 nm. The depletion length of typical CMOS imagers for color imaging is around 3-5 μm, the resulting QEs of 860 nm and 940 nm are only 14-23% and 6-11%, respectively. For outdoor use, the 940-nm wavelength is preferred to 860 nm because of the sunlight spectrum. For 940-nm wavelength, to achieve a good QE of > 80% requires > 70-μm depletion region. Therefore, expanding depleted regions is a key design point for TOF range imagers.

Using a lightly-doped epitaxial layer (at least in [25], [55]) is common and useful to increase the depletion region, which is available to use only the exchange of wafers. However, the channel potential of the charge modulator is limited to 1-2 V, the expansion of the depletion layer is insufficient to improve the NIR sensitivity.

Using a gradual-doping epitaxial layer [82] is one of the techniques to expand the depletion region. A built-in potential due to the difference of doping concentration en-
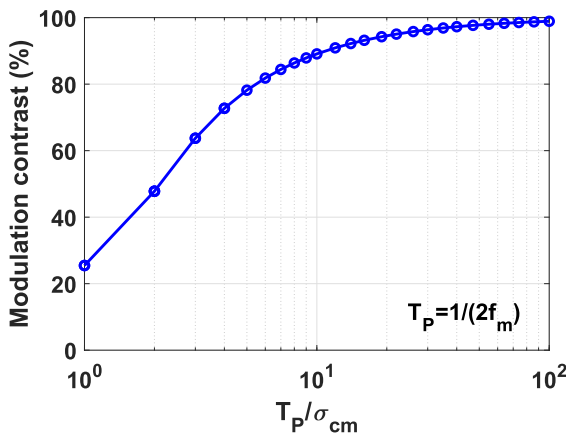

Fig. 8 Modulation contrast as function of T_P/σ_{cm}. The calculated modulation contrast is equivalent to 2-tap CW-iTOF where the modulation frequency is $f_m = 1/(2T_P)$.
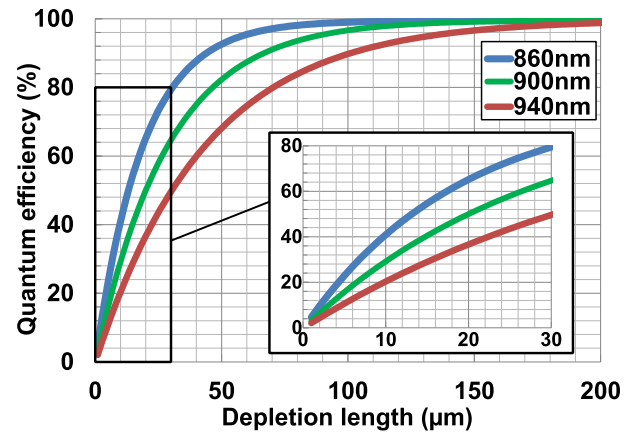

Fig. 9 Depletion length vs. QE for the wavelengths of 860, 900, 940 nm.
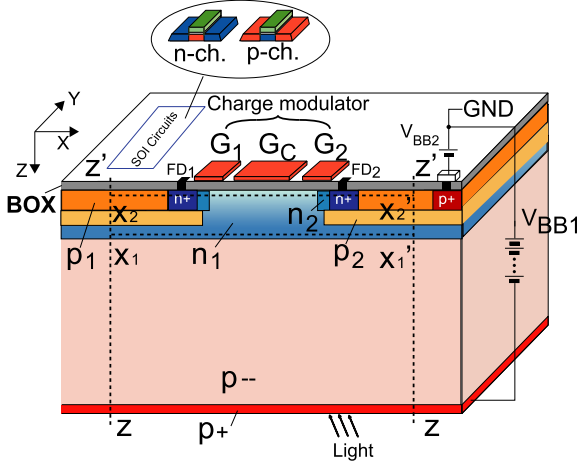
Fig. 10 SOI-based fully-depleted thick-substrate lock-in pixel.

larges the depletion region. However, the improvement is expected to be small because the potential difference, $\Delta\phi$, of two p-type laysers is calculated as

$$\Delta\phi = \frac{kT}{q} \ln \frac{N_{A1}}{N_{A2}} \tag{9}$$

where N_{A1} and N_{A2} is those respective doping concentrations. For example, the condition of $N_{A1}/N_{A2} = 10$ gives only $\Delta\phi \approx 60$ mV. In reality, although the structure [82] demonstrates a high-speed modulation of 160 MHz with 55% modulation contrast even at 930 nm, the QE is only 6% even at 850-nm wavelength.

The authors presented an SOI-based charge modulator with a fully-depleted thick substrate [24] in 2020. The conceptual structure is shown in Fig. 10. The modulation gates are formed using active layers on the buried oxide (BOX) that are usually used for a source/drain of SOI transistors. The paper first demonstrates charge modulation capability at 40-ns gate pulse using a fully-depleted thick substrate of >200 μm. To the best of the author's knowledge, it has achieved the highest QE of 55% at a 940-nm wavelength in TOF range image sensors. Since the limited QE is due to the loss caused by the parasitic sensitivity of FDs, further improvement on the QE is expected.

Recently, the authors also have proposed a LEFM-based charge modulator with substrate biasing [79], [83], [84]. The structure has a fully-depleted epitaxial layer with 13-μm thickness in the bulk CMOS that is highly compatible with standard CMOS image sensor technologies. The structure theoretically obtains a relatively high QE of 25% in a calculation while keeping high-speed modulation.

Enhancing NIR sensitivity using advanced technologies such as deep trench isolation (DTI) has also been presented [11], [12], [85]–[87]. They implement a scattering [11], [85], [86] or a diffraction [12], [87] structure at the backside surface to increase the angle of incident light. The DTI is also introduced to reduce optical crosstalk between pixels and to increase the QE with multiple reflections to enlarge photon-sensitive length. According to [86], the QE
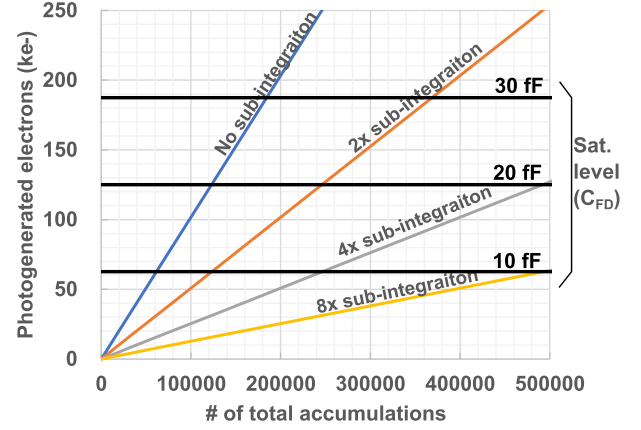

Fig. 11 Calculation results of photogenerated electrons due to 110-klx BGL.

Table 2 Calculation condition of the photogenerated electrons due to BGL

Parameter	Value
Wavelength	940 nm
Optical bandpass filter	40 nm
F number	1.4
QE	50%
Fill factor	50%
Pixel size	100 μm^2
Reflectivity of a target	0.8
T_P	10 ns
Signal swing	1.0 V

is improved from 20% to 32% at 940 nm using a pyramid-shaped structure for diffraction. In [11], the QE of 38% at 940 nm is obtained using the scattering structure.

4.2 BGL Suppression Technique

As demand for outdoor use increases, BGL suppression is becoming more critical. Figure 11 shows calculation results of the estimated photogenerated electrons due to the BGL (110 klx) where the condition is summarised in Table 2. Saturation levels under the various capacitances at the FD are also shown where the available signal swing is supposed to be 1 V. Under no BGL suppression, the saturation occurs immediately, and there is no room to accumulate signal electrons due to the laser pulse.

The basic idea of BGL suppression is to divide the integration in a frame into several sub-integrations. The simplest way is to do a readout for each sub-integration, which is equivalent to increasing the sensor's frame rate. However, limited readout noise induces at each readout, resulting in lower SNR as well as increasing power consumption. For this reason, in the actual implementation of BGL suppression, a common mode of signal charges or voltages between taps is canceled while the difference signal between taps is stored in pixel or column.

Bamji et.al [9] presented a pixel-level BGL suppression shown in Fig. 12. The concept is similar to [41] shown in Table 1. During the BGL suppression operation (ϕ_{CMR} on),
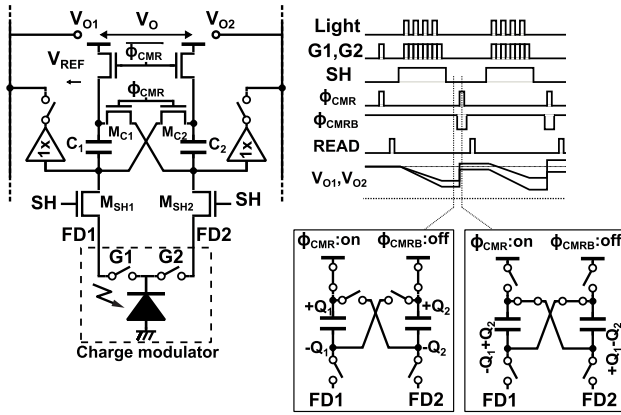
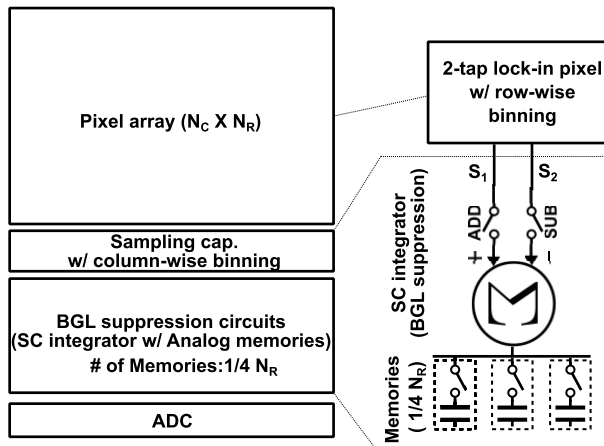Fig. 12   Pixel-level BGL suppression technique [9].

Fig. 13   Column-level BGL suppression technique [89].

the signal charges stored in two capacitors (C_1 and C_2) are summed up with opposite polarity. Therefore the common component due to BGL is canceled, and the differential signals only remain after this operation. This operation can be performed on all pixels at the same time. The advantage of this method is that kTC noises on M_{C1} and M_{C2} are also canceled out by taking the difference between taps. Hense the kTC noises are not integrated for each BGL suppression though the kTC noise on M_{SH} remains.

Another approach in pixel-level BGL suppression was presented [88]. The paper proposed a lock-in pixel with a polarity-switchable photodiode and a charge amplifier. The photodiode is composed of p+-n-well-p-sub structure where the p+ and p-sub layers are electrically separated, unlike the standard pinned photodiode. The diode with the p+-n-well enables the treatment of both photogenerated holes and electrons. Those charges are accumulated into the charge amplifier by switching the polarity. Since the dominant sensitivity of photodiode is determined by the n-well-p-sub diode, the BGL cancelation effect is limited. Though, with the proposed diode and sub-frame readout scheme, the paper demonstrates the BGL suppression capability up to 180 klx.

Column-level BGL suppression shown in Fig. 13 is

presented in [89]. In the BGL suppression, the difference between taps is taken by an SC integrator implemented in the column readout, and the differential signal is stored into analog memories in the column. After this operation, FDs in the pixel are reset, and another sub-integration begins. The operation is performed row by row. This method does not require a large capacitor in the pixel; it is suitable for small pixels. Obviously, this method requires analog memories as many as the number of pixel rows in every column. For relaxing the requirement, the paper [89] uses 4×4 pixel binning, and a super-resolution technique using shifted binning pixels is used to recover spatial resolution. As a result, the number of required analog memories is reduced to 1/16 of the pixel array. In [71], the analog memories are implemented in each pixel using MIM capacitors. The fill factor is not worse owing to adapting the BSI structure. In column-level BGL suppression, the kT/C noises that are induced at the sampling on analog memories are summed up at each sub-integration. The influence of the kT/C noises on the depth calculation depends on the BGL level; the kT/C noise becomes dominant at a weak BGL while they are negligible at a strong BGL due to its shot noise.

5.   Conclusion

In this paper, iTOF range imagers reported over the past two decades are reviewed and discussed to give an overview of iTOF sensor design. The performance of TOF cameras has improved remarkably in terms of spatial resolution and depth precision. For more applications, outdoor and long-distance imaging and low power consumption characteristics will be important. As for coming decade, the continuous evolution of this sensor technology is highly expected.

Acknowledgments

References

[1] R. Lange and P. Seitz, "Solid-state time-of-flight range camera," IEEE Journal of Quantum Electronics, vol.37, no.3, pp.390–397, March 2001.

[2] C. Niclass, A. Rochas, P.-A. Besse, and E. Charbon, "Design and characterization of a CMOS 3-D image sensor based on single photon avalanche diodes," IEEE Journal of Solid-State Circuits, vol.40, no.9, pp.1847–1854, Sept. 2005.

[3] C. Niclass, M. Soga, H. Matsubara, M. Ogawa, and M. Kagami, "A 0.18-μm CMOS SoC for a 100-m-Range 10-Frame/s 200 × 96-Pixel Time-of-Flight Depth Sensor," IEEE Journal of Solid-State Circuits, vol.49, no.1, pp.315–330, Jan. 2014.

[4] A.R. Ximenes, P. Padmanabhan, M.-J. Lee, Y. Yamashita, D.N. Yaung, and E. Charbon, "A 256 × 256 45/65nm 3D-stacked SPAD-based direct TOF image sensor for LiDAR applications with optical polar modulation for up to 18.6dB interference suppression," 2018 IEEE International Solid - State Circuits Conference -

(ISSCC), pp.96–98, Feb. 2018.

[5] D. Bronzi, F. Villa, S. Tisa, A. Tosi, and F. Zappa, "SPAD Figures of Merit for Photon-Counting, Photon-Timing, and Imaging Applications: A Review," IEEE Sensors Journal, vol.16, no.1, pp.3–12, Jan. 2016.

[6] O. Kumagai, J. Ohmachi, M. Matsumura, S. Yagi, K. Tayu, K. Amagawa, T. Matsukawa, O. Ozawa, D. Hirono, Y. Shinozuka, R. Homma, K. Mahara, T. Ohyama, Y. Morita, S. Shimada, T. Ueno, A. Matsumoto, Y. Otake, T. Wakano, and T. Izawa, "A 189×600 Back-Illuminated Stacked SPAD Direct Time-of-Flight Depth Sensor for Automotive LiDAR Systems," 2021 IEEE International Solid- State Circuits Conference (ISSCC), pp.110–112, Feb. 2021.

[7] F. Piron, D. Morrison, M.R. Yuce, and J.M. Redouté, "A Review of Single-Photon Avalanche Diode Time-of-Flight Imaging Sensor Arrays," IEEE Sensors Journal, vol.21, no.11, pp.12654–12666, June 2021.

[8] T. Spirig, P. Seitz, O. Vietze, and F. Heitger, "The lock-in CCD-two-dimensional synchronous detection of light," IEEE Journal of Quantum Electronics, vol.31, no.9, pp.1705–1708, Sept. 1995.

[9] C.S. Bamji, P. O'Connor, T. Elkhatib, S. Mehta, B. Thompson, L.A. Prather, D. Snow, O.C. Akkaya, A. Daniel, A.D. Payne, T. Perry, M. Fenton, and V.-H. Chan, "A 0.13 μm CMOS System-on-Chip for a 512×424 Time-of-Flight Image Sensor With Multi-Frequency Photo-Demodulation up to 130 MHz and 2 GS/s ADC," IEEE Journal of Solid-State Circuits, vol.50, no.1, pp.303–319, Jan. 2015.

[10] C.S. Bamji, S. Mehta, B. Thompson, T. Elkhatib, S. Wurster, O. Akkaya, A. Payne, J. Godbaz, M. Fenton, V. Rajasekaran, L. Prather, S. Nagaraja, V. Mogallapu, D. Snow, R. McCauley, M. Mukadam, I. Agi, S. McCarthy, Z. Xu, T. Perry, W. Qian, V.-H. Chan, P. Adepu, G. Ali, M. Ahmed, A. Mukherjee, S. Nayak, D. Gampell, S. Acharya, L. Kordus, and P. O'Connor, "IMpixel 65nm BSI 320MHz demodulated TOF Image sensor with 3μm global shutter pixels and analog binning," 2018 IEEE International Solid - State Circuits Conference - (ISSCC), pp.94–96, Feb. 2018.

[11] M.-S. Keel, D. Kim, Y. Kim, M. Bae, M. Ki, B. Chung, S. Son, H. Lee, H. Jo, S.-C. Shin, S. Hong, J. An, Y. Kwon, S. Seo, S. Cho, Y. Kim, Y.-G. Jin, Y. Oh, Y. Kim, J. Ahn, K. Koh, and Y. Park, "7.1 A 4-tap 3.5 μm 1.2 Mpixel Indirect Time-of-Flight CMOS Image Sensor with Peak Current Mitigation and Multi-User Interference Cancellation," 2021 IEEE International Solid- State Circuits Conference (ISSCC), San Francisco, CA, USA, pp.106–108, IEEE, Feb. 2021.

[12] Y. Ebiko, H. Yamagishi, K. Tatani, H. Iwamoto, Y. Moriyama, Y. Hagiwara, S. Maeda, T. Murase, T. Suwa, H. Arai, Y. Isogai, S. Hida, S. Kameda, T. Terada, K. Koiso, F.T. Brady, S. Han, A. Basavalingappa, T. Michiel, and T. Ueno, "Low power consumption and high resolution 1280X960 Gate Assisted Photonic Demodulator pixel for indirect Time of flight," 2020 IEEE International Electron Devices Meeting (IEDM), San Francisco, CA, USA, pp.33.1.1–33.1.4, IEEE, Dec. 2020.

[13] K. Yasutomi, Y. Okura, K. Kagawa, and S. Kawahito, "A Sub-100 μm-Range-Resolution Time-of-Flight Range Image Sensor With Three-Tap Lock-In Pixels, Non-Overlapping Gate Clock, and Reference Plane Sampling," IEEE Journal of Solid-State Circuits, vol.54, no.8, pp.2291–2303, Aug. 2019.

[14] R. Miyagawa and T. Kanade, "CCD-based range-finding sensor," IEEE Transactions on Electron Devices, vol.44, no.10, pp.1648–1652, Oct. 1997.

[15] D. Stoppa, N. Massari, L. Pancheri, M. Malfatti, M. Perenzoni, and L. Gonzo, "A Range Image Sensor Based on 10- μm Lock-In Pixels in 0.18-μm CMOS Imaging Technology," IEEE Journal of Solid-State Circuits, vol.46, no.1, pp.248–258, Jan. 2011.

[16] Y. Kato, T. Sano, Y. Moriyama, S. Maeda, T. Yamazaki, A. Nose, K. Shiina, Y. Yasu, W. van der Tempel, A. Ercan, Y. Ebiko, D.V. Nieuwenhove, and S. Sukegawa, "320 × 240 Back-Illuminated 10- μm CAPD Pixels for High-Speed Modulation Time-of-Flight CMOS Image Sensor," IEEE Journal of Solid-State Circuits, vol.53,

[17] no.4, pp.1071–1078, April 2018.

[17] M.-S. Keel, Y.-G. Jin, Y. Kim, D. Kim, Y. Kim, M. Bae, B. Chung, S. Son, H. Kim, T. An, S.-H. Choi, T. Jung, Y. Kwon, S. Seo, S.-Y. Kim, K. Bae, S.-C. Shin, M. Ki, S. Yoo, C.-R. Moon, H. Ryu, and J. Kim, "A VGA Indirect Time-of-Flight CMOS Image Sensor With 4-Tap 7- μ m Global-Shutter Pixel and Fixed-Pattern Phase Noise Self-Compensation," IEEE Journal of Solid-State Circuits, vol.55, no.4, pp.889–897, April 2020.

[18] A.P.P. Jongenelen, D.G. Bailey, A.D. Payne, A.A. Dorrington, and D.A. Carnegie, "Analysis of Errors in ToF Range Imaging With Dual-Frequency Modulation," IEEE Transactions on Instrumentation and Measurement, vol.60, no.5, pp.1861–1868, May 2011.

[19] A.D. Payne, A.P.P. Jongenelen, A.A. Dorrington, M.J. Cree, and D.A. Carnegie, "Multiple frequency range imaging to remove measurement ambiguity," Optical 3-D Measurement Techniques, 2009.

[20] R. Whyte, "Phase Wrapping and its Solution in Time-of-Flight Depth Sensing." https://medium.com/chronoptics-time-of-flight/phase-wrapping-and-its-solution-in-time-of-flight-depth-sensing-493aa8b21c42, Nov. 2020.

[21] T. Sawada, K. Ito, M. Nakayama, and S. Kawahito, "TOF range image sensor using a range-shift technique," 2008 IEEE SENSORS, pp.1390–1393, Oct. 2008.

[22] T. Kasugai, S.-M. Han, H. Trang, T. Takasawa, S. Aoyama, K. Yasutomi, K. Kagawa, and S. Kawahito, "A Time-of-Flight CMOS Range Image Sensor Using 4-Tap Output Pixels with Lateral-Electric-Field Control," Electronic Imaging, vol.2016, no.12, pp.1–6, Feb. 2016.

[23] Y. Shirakawa, K. Yasutomi, K. Kagawa, S. Aoyama, and S. Kawahito, "An 8-Tap CMOS Lock-In Pixel Image Sensor for Short-Pulse Time-of-Flight Measurements," Sensors, vol.20, no.4, p.1040, Feb. 2020.

[24] S. Lee, K. Yasutomi, M. Morita, H. Kawanishi, and S. Kawahito, "A Time-of-Flight Range Sensor Using Four-Tap Lock-In Pixels with High near Infrared Sensitivity for LiDAR Applications," Sensors, vol.20, no.1, p.116, March 2020.

[25] S. Kawahito, I.A. Halin, T. Ushinaga, T. Sawada, M. Homma, and Y. Maeda, "A CMOS Time-of-Flight Range Image Sensor With Gates-on-Field-Oxide Structure," IEEE Sensors Journal, vol.7, no.12, pp.1578–1586, Dec. 2007.

[26] Y. Kwon, S. Seo, S. Cho, S.-H. Choi, T. Hwang, Y. Kim, Y.-G. Jin, Y. Oh, M.-S. Keel, D. Kim, M. Bae, Y. Km, S.-C. Shin, S. Hong, S.-H. Lee, H.W. Park, Y. Kim, K. Koh, and J. Ahn, "A 2.8 μm Pixel for Time of Flight CMOS Image Sensor with 20 ke-Full-Well Capacity in a Tap and 36 % Quantum Efficiency at 940 nm Wavelength," 2020 IEEE International Electron Devices Meeting (IEDM), San Francisco, CA, USA, pp.33.2.1–33.2.4, IEEE, Dec. 2020.

[27] R. Miyagawa and T. Kanade, "Integration-time based computational image sensors," 1995 IEEE Workshop on CCDs and Advanced Image Sensors, April 1995.

[28] T. Spirig, M. Marley, and P. Seitz, "The multitap lock-in CCD with offset subtraction," IEEE Transactions on Electron Devices, vol.44, no.10, pp.1643–1647, Oct. 1997.

[29] E.R. Fossum, "CMOS image sensors: Electronic camera-on-a-chip," IEEE Transactions on Electron Devices, vol.44, no.10, pp.1689–1698, Oct. 1997.

[30] R. Schwarte, Z. Xu, H.-G. Heinol, J. Olk, R. Klein, B. Buxbaum, H. Fischer, and J. Schulte, "New electro-optical mixing and correlating sensor: Facilities and applications of the photonic mixer device (PMD)," Sensors, Sensor Systems, and Sensor Data Processing, pp.245–253, International Society for Optics and Photonics, Sept. 1997.

[31] S.B. Gokturk, H. Yalcin, and C. Bamji, "A Time-Of-Flight Depth Sensor - System Description, Issues and Solutions," 2004 Conference on Computer Vision and Pattern Recognition Workshop, pp.35–35, June 2004.

[32] R. Jeremias, W. Brockherde, G. Doemens, B. Hosticka, L. Listl, and P. Mengel, "A CMOS photosensor array for 3D imaging us-

ing pulsed laser," 2001 IEEE International Solid-State Circuits Conference. Digest of Technical Papers. ISSCC (Cat. No.01CH37177), pp.252–253, Feb. 2001.

[33] F. Remondino and D. Stoppa, eds., TOF Range-Imaging Cameras, Springer, Berlin, Heidelberg, 2013.

[34] O. Elkhalili, O.M. Schrey, P. Mengel, M. Petermann, W. Brockherde, and B.J. Hosticka, "A 4/spl times/64 pixel CMOS image sensor for 3-D measurement applications," IEEE Journal of Solid-State Circuits, vol.39, no.7, pp.1208–1212, July 2004.

[35] D. Stoppa, L. Viarani, A. Simoni, L. Gonzo, M. Malfatti, and G. Pedretti, "A 50x30-pixel CMOS sensor for TOF-based real time 3D imaging," Proceedings of IEEE Workshop on CCDs and Adv. Image Sensors, pp.230–233, June 2005.

[36] D. Stoppa, L. Viarani, A. Simoni, L. Gonzo, M. Malfatti, and G. Pedretti, "A 16/spl times/16-pixel range-finding CMOS image sensor," Proceedings of the 30th European Solid-State Circuits Conference, pp.419–422, Sept. 2004.

[37] Y. Oike, M. Ikeda, and K. Asada, "Pixel-level color image sensor with efficient ambient light suppression using modulated RGB flashlight and application to TOF range finding," 2004 Symposium on VLSI Circuits. Digest of Technical Papers (IEEE Cat. No.04CH37525), pp.298–301, June 2004.

[38] M. Perenzoni, N. Massari, D. Stoppa, L. Pancheri, M. Malfatti, and L. Gonzo, "A 160×120-Pixels Range Camera With In-Pixel Correlated Double Sampling and Fixed-Pattern Noise Correction," IEEE Journal of Solid-State Circuits, vol.46, no.7, pp.1672–1681, July 2011.

[39] G. Zach, M. Davidovic, and H. Zimmermann, "Extraneous-light resistant multipixel range sensor based on a low-power correlating pixel-circuit," 2009 Proceedings of ESSCIRC, pp.236–239, Sept. 2009.

[40] G. Zach and H. Zimmermann, "A 2×32 range-finding sensor array with pixel-inherent suppression of ambient light up to 120klx," 2009 IEEE International Solid-State Circuits Conference - Digest of Technical Papers, pp.352–353, 353a, Feb. 2009.

[41] G. Zach, M. Davidovic, and H. Zimmermann, "A 16×16 Pixel Distance Sensor With In-Pixel Circuitry That Tolerates 150 klx of Ambient Light," IEEE Journal of Solid-State Circuits, vol.45, no.7, pp.1345–1353, July 2010.

[42] S. Ando and A. Kimachi, "Time-domain correlation image sensor: First CMOS realization of demodulator pixels array," Proc. 1999 IEEE Workshop on CCDs and Advanced Image Sensors, pp.33–36, June 1999.

[43] S. Ando and A. Kimachi, "Correlation image sensor: Two-dimensional matched detection of amplitude-modulated light," IEEE Transactions on Electron Devices, vol.50, no.10, pp.2059–2066, Oct. 2003.

[44] J. Ohta, K. Yamamoto, T. Hirai, K. Kagawa, M. Nunoshita, M. Yamada, Y. Yamasaki, S. Sugishita, and K. Watanabe, "An image sensor with an in-pixel demodulation function for detecting the intensity of a modulated light signal," IEEE Transactions on Electron Devices, vol.50, no.1, pp.166–172, Jan. 2003.

[45] T.Y. Lee, Y. Lee, D.K. Min, J. Lee, Y.G. Jin, Y. Park, C. Chung, I. Ovsiannikov, and E.R. Fossum, "Dark current suppression during high speed photogate modulation for 3D ToF imaging pixel," 2011 International Image Sensor Workshop, p.R17, June 2011.

[46] T.-Y. Lee, Y.-J. Lee, D.-K. Min, S.-H. Lee, W.-H. Kim, J.-K. Jung, I. Ovsiannikov, Y.-G. Jin, Y. Park, and E.R. Fossum, "A Time-of-Flight 3-D Image Sensor With Concentric-Photogates Demodulation Pixels," IEEE Transactions on Electron Devices, vol.61, no.3, pp.870–877, March 2014.

[47] C. Tubert, L. Simony, F. Roy, A. Tournier, L. Pinzelli, and P. Magnan, "High speed dual port pinned-photodiode for time-of-flight imaging," 2009 International Image Sensor Workshop, p.3, June 2009.

[48] S.-J. Kim, S.-W. Han, B. Kang, K. Lee, J.D.K. Kim, and C.-Y. Kim, "A Three-Dimensional Time-of-Flight CMOS Image Sensor With

Pinned-Photodiode Pixel Structure," IEEE Electron Device Letters, vol.31, no.11, pp.1272–1274, Nov. 2010.

[49] S.-J. Kim, "Performance Evaluation of Pinning Potential Adjustment in Two-Dimensional/Three-Dimensional Image Sensor," IEEE Electron Device Letters, vol.33, no.10, pp.1426–1428, Oct. 2012.

[50] S.-J. Kim, J.D.K. Kim, B. Kang, and K. Lee, "A CMOS Image Sensor Based on Unified Pixel Architecture With Time-Division Multiplexing Scheme for Color and Depth Image Acquisition," IEEE Journal of Solid-State Circuits, vol.47, no.11, pp.2834–2845, Nov. 2012.

[51] N. Teranishi, A. Kohono, Y. Ishihara, E. Oda, and K. Arai, "No image lag photodiode structure in the interline CCD image sensor," 1982 International Electron Devices Meeting, pp.324–327, Dec. 1982.

[52] N. Teranishi, "Effect and Limitation of Pinned Photodiode," IEEE Transactions on Electron Devices, vol.63, no.1, pp.10–15, Jan. 2016.

[53] E.R. Fossum and D.B. Hondongwa, "A Review of the Pinned Photodiode for CCD and CMOS Image Sensors," IEEE Journal of the Electron Devices Society, vol.2, no.3, pp.33–43, May 2014.

[54] S. Kawahito, G. Baek, Z. Li, S.M. Han, M.W. Seo, K. Yasutomi, and K. Kagawa, "CMOS lock-in pixel image sensors with lateral eelectric field cotrol for time-resolved imaging," 2013 International Image Sensor Workshop, pp.361–364, June 2013.

[55] S.-M. Han, T. Takasawa, K. Yasutomi, S. Aoyama, K. Kagawa, and S. Kawahito, "A Time-of-Flight Range Image Sensor With Background Canceling Lock-in Pixels Based on Lateral Electric Field Charge Modulation," IEEE Journal of the Electron Devices Society, vol.3, no.3, pp.267–275, May 2015.

[56] S. Kawahito, Z. Li, and K. Yasutomi, "A CMOS image sensor with draining only modulation pixels for sub-nanosecond time-resolved imaging," 2011 International Image Sensor Workshop, pp.R21–1–4, June 2011.

[57] Z. Li, S. Kawahito, K. Yasutomi, K. Kagawa, J. Ukon, M. Hashimoto, and H. Niioka, "A Time-Resolved CMOS Image Sensor With Draining-Only Modulation Pixels for Fluorescence Lifetime Imaging," IEEE Transactions on Electron Devices, vol.59, no.10, pp.2715–2722, Oct. 2012.

[58] K. Yasutomi, T. Usui, S.-M. Han, T. Takasawa, K. Kagawa, and S. Kawahito, "An indirect time-of-flight measurement technique with impulse photocurrent response for sub-millimeter range resolved imaging," Optics Express, vol.22, no.16, pp.18904–18913, Aug. 2014.

[59] K. Yasutomi, T. Usui, S.M. Han, T. Takasawa, K. Kagawa, and S. Kawahito, "A submillimeter range resolution time-of-flight range imager with column-wise skew calibration," IEEE Transactions on Electron Devices, vol.63, no.1, pp.182–188, Jan. 2016.

[60] M.W. Seo, K. Kagawa, K. Yasutomi, Y. Kawata, N. Teranishi, Z. Li, I.A. Halin, and S. Kawahito, "A 10 ps time-resolution CMOS image sensor with two-tap true-CDS lock-in pixels for fluorescence lifetime imaging," IEEE Journal of Solid-State Circuits, vol.51, no.1, pp.141–154, Jan. 2016.

[61] M.W. Seo, Y. Shirakawa, Y. Kawata, K. Kagawa, K. Yasutomi, and S. Kawahito, "A time-resolved four-tap lock-in pixel CMOS image sensor for real-time fluorescence lifetime imaging microscopy," IEEE Journal of Solid-State Circuits, vol.53, no.8, pp.2319–2330, Aug. 2018.

[62] D. Van Nieuwenhove, W. van der Tempel, R. Grootjans, J. Stiens, and M. Kuijk, "Photonic Demodulator With Sensitivity Control," IEEE Sensors Journal, vol.7, no.3, pp.317–318, March 2007.

[63] G.-F.D. Betta, S. Donati, Q.D. Hossain, G. Martini, L. Pancheri, D. Saguatti, D. Stoppa, and G. Verzellesi, "Design and Characterization of Current-Assisted Photonic Demodulators in 0.18- μm CMOS Technology," IEEE Transactions on Electron Devices, vol.58, no.6, pp.1702–1709, June 2011.

[64] Y. Kato, T. Sano, Y. Moriyama, S. Maeda, T. Yamazaki, A. Nose, K. Shina, Y. Yasu, W. van der Tempel, A. Ercan, and Y. Ebiko, "320×240 Back-illuminated $10\mu m$ CAPD pixels for high speed

modulation Time-of-Flight CMOS image sensor," 2017 Symposium on VLSI Circuits, pp.C288–C289, June 2017.

[65] S. Kawahito, K. Kondo, K. Yasutomi, and K. Kagawa, "A time-resolved lock-in pixel image sensor using multiple-tapped diode and hybrid cascade charge transfer structures," 2019 International Image Sensor Workshop, p.R28, June 2019.

[66] H. Nagae, S. Daikoku, K. Kondo, K. Yasutomi, K. Kagawa, and S. Kawahito, "A time-resolved 4-tap image sensor using tapped PN-junction diode demodulation pixels," 2021 International Image Sensor Workshop, p.4, 2021-9, In press.

[67] B. Buttgen, F. Lustenberger, and P. Seitz, "Demodulation Pixel Based on Static Drift Fields," IEEE Transactions on Electron Devices, vol.53, no.11, pp.2741–2747, Nov. 2006.

[68] K. Kondo, K. Yasutomi, K. Yamada, A. Komazawa, Y. Handa, Y. Okura, T. Michiba, S. Aoyama, and S. Kawahito, "A Built-in Drift-field PD Based 4-tap Lock-in Pixel for Time-of-Flight CMOS Range Image Sensors," Extended Abstracts of the 2018 International Conference on Solid State Devices and Materials, Hongo Campus, The University of Tokyo, Tokyo, Japan, The Japan Society of Applied Physics, Sept. 2018.

[69] H. Takeshita, T. Sawada, T. Iida, K. Yasutomi, and S. Kawahito, "High-speed charge transfer pinned-photodiode for a CMOS time-of-flight range image sensor," IS&T/SPIE Electronic Imaging, ed. E. Bodegom and V. Nguyen, San Jose, California, p.75360R, Feb. 2010.

[70] S. Lee, D. Park, S. Lee, J. Choi, and S.-J. Kim, "Design of a Time-of-Flight Sensor With Standard Pinned-Photodiode Devices Toward 100-MHz Modulation Frequency," IEEE Access, vol.7, pp.130451–130459, 2019.

[71] D. Kim, S. Lee, D. Park, C. Piao, J. Park, Y. Ahn, K. Cho, J. Shin, S.M. Song, S.-J. Kim, J.-H. Chun, and J. Choi, "Indirect Time-of-Flight CMOS Image Sensor With On-Chip Background Light Cancelling and Pseudo-Four-Tap/Two-Tap Hybrid Imaging for Motion Artifact Suppression," IEEE Journal of Solid-State Circuits, vol.55, no.11, pp.2849–2865, Nov. 2020.

[72] E. Tadmor, A. Lahav, G. Yahav, A. Fish, and D. Cohen, "A Fast-Gated CMOS Image Sensor With a Vertical Overflow Drain Shutter Mechanism," IEEE Transactions on Electron Devices, vol.63, no.1, pp.138–144, Jan. 2016.

[73] E. Tadmor, D. Cohen, G. Yahav, G. Tennenholtz, G. Lehana, A. Lahav, A. Birman, A. Fenigstein, and A. Fish, "Development of a ToF Pixel With VOD Shutter Mechanism, High IR QE, Four Storages, and CDS," IEEE Transactions on Electron Devices, vol.63, no.7, pp.2892–2899, July 2016.

[74] T.G. Etoh, A.Q. Nguyen, Y. Kamakura, K. Shimonomura, T.Y. Le, and N. Mori, "The Theoretical Highest Frame Rate of Silicon Image Sensors," Sensors, vol.17, no.3, p.483, March 2017.

[75] K. Yasutomi, S. Itoh, and S. Kawahito, "A 2.7e- temporal noise 99.7% shutter efficiency 92dB dynamic range CMOS image sensor with dual global shutter pixels," 2010 IEEE International Solid-State Circuits Conference - (ISSCC), pp.398–399, Feb. 2010.

[76] M. Sakakibara, Y. Oike, T. Takatsuka, A. Kato, K. Honda, T. Taura, T. Machida, J. Okuno, A. Ando, T. Fukuro, T. Asatsuma, S. Endo, J. Yamamoto, Y. Nakano, T. Kaneshige, I. Yamamura, T. Ezaki, and T. Hirayama, "An 83dB-dynamic-range single-exposure global-shutter CMOS image sensor with in-pixel dual storage," 2012 IEEE International Solid-State Circuits Conference, pp.380–382, Feb. 2012.

[77] C. Cao, Y. Shirakawa, L. Tan, M.-W. Seo, K. Kagawa, K. Yasutomi, T. Kosugi, S. Aoyama, N. Teranishi, N. Tsumura, and S. Kawahito, "A Two-Tap NIR Lock-in Pixel CMOS Image Sensor with Background Light Cancelling Capability for Non-Contact Heart Rate Detection," 2018 IEEE Symposium on VLSI Circuits, pp.75–76, June 2018.

[78] H. Eltoukhy, K. Salama, and A. ElGamal, "A 0.18-/spl mu/m CMOS Bioluminescence Detection Lab-on-Chip," IEEE Journal of Solid-State Circuits, vol.41, no.3, pp.651–662, March 2006.

[79] K. Yasutomi, M. Inoue, S. Daikoku, K. Mars, and S. Kawahito, "A

4-tap lock-in pixel time-of-flight range imager with substrate biasing and double-delta correlated multiple sampling," 2021 International Image Sensor Workshop, 2021-9, In press.

[80] S. Adachi, W. Lee, N. Akahane, H. Oshikubo, K. Mizobuchi, and S. Sugawa, "A 200-μV/e$^-$ CMOS Image Sensor With 100-ke$^-$ Full Well Capacity," IEEE Journal of Solid-State Circuits, vol.43, no.4, pp.823–830, April 2008.

[81] Y. Fujihara, M. Murata, S. Nakayama, R. Kuroda, and S. Sugawa, "An Over 120 dB Single Exposure Wide Dynamic Range CMOS Image Sensor With Two-Stage Lateral Overflow Integration Capacitor," IEEE Transactions on Electron Devices, vol.68, no.1, pp.152–157, Jan. 2021.

[82] B. Rodrigues, M. Guillon, N. Billon-Pierron, J.B. Mancini, B. Giffard, Y. Cazaux, P. Malinge, P. Waltz, A. Ngoua, A. Taluy, S. Kuster, S. Joblot, F. Roy, and G.N. Lu, "Indirect ToF pixel integrating fast buried-channel transfer gates and gradual epitaxy, and enabling CDS," 2017 International Image Sensor Workshop, pp.266–269, 2017ê.

[83] M. Inoue, S. Daikoku, K. Kondo, A. Komazawa, K. Mars, K. Yasutomi, K. Kagawa, and S. Kawahito, "A short-pulse based time-of-flight image sensor using 4-tap charge-modulation pixels with accelerated carrier response," ITE Technical Report; ITE Tech. Rep., vol.44, no.11, pp.25–28, March 2020.

[84] M. Inoue, S. Daikoku, K. Kondo, A. Komazawa, K. Mars, K. Yasutomi, K. Kagawa, and S. Kawahito, "A short-pulse based time-of-flight image sensor using 4-tap charge-modulation pixels with accelerated carrier response," ITE Technical Report; ITE Tech. Rep., pp.25–28, ITE (In Japanese), March 2020.

[85] J. Park, Y. Lee, B. Kim, B. Kim, J. Park, E. Yeom, Y. Jung, T. Kim, H. Yoon, Y. Kim, J. Park, C.R. Moon, and Y. Park, "Pixel technology for improving IR quantum efficiency of backside- illuminated CMOS image sensor," 2019 International Image Sensor Workshop, p.R14, June 2019.

[86] T. Jung, Y. Kwon, S. Seo, M.-S. Keel, C. Lee, S.-H. Choi, S.-Y. Kim, S. Cho, Y. Kim, Y.-G. Jin, M. Lim, H. Ryu, Y. Kim, J. Kim, and C.-R. Moon, "A 4-tap global shutter pixel with enhanced IR sensitivity for VGA time-of-flight CMOS image sensors," Electronic Imaging 2020, pp.103-1–103-6, Jan. 2020.

[87] S. Yokogawa, I. Oshiyama, H. Ikeda, Y. Ebiko, T. Hirano, S. Saito, T. Oinoue, Y. Hagimoto, and H. Iwamoto, "IR sensitivity enhancement of CMOS Image Sensor with diffractive light trapping pixels," Scientific Reports, vol.7, no.1, p.3832, Dec. 2017.

[88] T.-H. Hsu, T. Liao, N.-A. Lee, and C.-C. Hsieh, "A CMOS Time-of-Flight Depth Image Sensor With In-Pixel Background Light Cancellation and Phase Shifting Readout Technique," IEEE Journal of Solid-State Circuits, vol.53, no.10, pp.2898–2905, Oct. 2018.

[89] J. Cho, J. Choi, S.-J. Kim, S. Park, J. Shin, J.D.K. Kim, and E. Yoon, "A 3-D Camera With Adaptable Background Light Suppression Using Pixel-Binning and Super-Resolution," IEEE Journal of Solid-State Circuits, vol.49, no.10, pp.2319–2332, Oct. 2014.

Keita Yasutomi received the Ph.D. degree from Shizuoka University, Hamamatsu, Japan, in 2011. Since 2021, he has been an Associate Professor with the Research Institute of Electronics, Shizuoka University. He is a member of the ITE, IEICE, and IEEE. His research interests include time-resolved CMOS image sensors and low-noise imagers.

Shoji Kawahito received the received the Ph.D. degree from Tohoku University, Sendai, Japan, in 1988. He has been a Professor with the Research Institute of Electronics, Shizuoka University, Shizuoka, Japan, since 1999. His current research interests include CMOS imaging devices, sensor interface circuits, and mixed analog/digital circuits designs.